

Polar EuO(111) on Ir(111): A two-dimensional oxideStefan Schumacher,^{1,*} Daniel F. Förster,¹ Feiming Hu,² Thomas Frauenheim,² Tim O. Wehling,^{2,3} and Thomas Michely¹¹*II. Physikalisches Institut, Universität zu Köln, Zùlpicher Straße 77, 50937 Köln, Germany*²*BCCMS, Universität Bremen, Am Fallturm 1a, 28359 Bremen, Germany*³*Institut für Theoretische Physik, Universität Bremen, Otto-Hahn-Allee 1, 28359 Bremen, Germany*

(Received 10 January 2014; revised manuscript received 17 February 2014; published 11 March 2014)

Through reactive molecular-beam epitaxy or Eu postoxidation and postannealing, large EuO(111) bilayer islands of high quality and exceptional stability are grown on Ir(111). We use scanning tunneling microscopy, low-energy electron diffraction, magneto-optical Kerr effect measurements, and density functional theory to characterize the properties of this ultrathin polar rare-earth metal oxide in atomistic detail. We analyze the crystallographic properties and their growth dependence, the film morphology including the atomic structure of defects, the mechanisms for reduction in the electrostatic potential related to the film polarity, as well as the work function, thermal stability, and magnetic properties, resulting in a comprehensive picture of this new two-dimensional material.

DOI: [10.1103/PhysRevB.89.115410](https://doi.org/10.1103/PhysRevB.89.115410)

PACS number(s): 68.47.Gh, 68.55.-a, 73.30.+y, 68.37.Ef

I. INTRODUCTION

In ionic crystals, surface orientations terminating alternate layers of positively and negatively charged ions are called *polar surfaces* [1] and have been a subject of intense work for the past decades [2–4]. As the elementary building blocks are double layers, each bearing a net dipole moment, their consecutive stacking would result in an infinite increase in the electrostatic potential such that the surface energy diverges. Evidently, such ideal polar surfaces with the structure of the truncated bulk cannot exist. Nevertheless, polar surfaces can be prepared in experiment as nature avoids the truncated bulk situation through a variety of structural and electronic surface modifications that supply compensating surface charges [2]. Such modifications include, for example, adsorption of light elements [5], adsorption of hydroxyl groups [6,7], and severe surface reconstructions [8,9].

In ultrathin polar films, the electrostatic contribution to the surface energy does not diverge. The number of double layers is limited, with the low thickness limit being just a single bilayer. Correspondingly, the existence of uncompensated polarity has been theoretically predicted for ultrathin polar films [10]. However, such uncompensated polarity has not yet been confirmed experimentally. Up to now, it was invariably found that also in ultrathin polar films a lowering of the energy associated with the dipole layer takes place. To mention a few examples, for the FeO(111) bilayer on Pt(111), a strong reduction in the interlayer spacing was measured [11,12], for the MgO(111) bilayer on Ag(111), an in-plane expansion reducing the surface charge density as well as a metallization of the bilayer was reported [13], and for the NaCl(111) trilayer on Al(111), a change in the ionic valence state of the Na ions was calculated [14].

Whereas, in the past, ultrathin polar oxide bilayers based on a variety of transition metals, such as Fe [15], Co [16], Ti [17], Zn [18], etc., and alkaline-earth metals, such as Mg [19] have been grown and have been investigated successfully, here the properties of a rare-earth polar oxide bilayer are investigated.

It is of specific interest to compare whether rare-earth polar oxide bilayers display new mechanisms to compensate the film polarity and in which respect their properties are similar to the ones of polar alkaline-earth or transition-metal oxides.

With this in view, we investigate the growth of the rare-earth metal-oxide EuO, which crystallizes in the rock-salt structure. The (111) planes consist of alternate layers of cationic Eu^{2+} and anionic O^{2-} ions so that EuO(111) is the lowest index polar orientation. EuO belongs to the rare class of ferromagnetic semiconductors and has a Curie temperature of $T_C = 69$ K. Whereas the band gap is 1.1 eV above T_C [20], EuO shows, upon appropriate doping, a semiconductor-to-metal transition when cooling below T_C [21]. Due to its high spin polarization in the ferromagnetic state [22], EuO is an attractive material for semiconductor-based spintronic devices [23,24]. The investigation of its polar orientation is of special interest as the electronic and magnetic properties of polar bilayers are expected to differ strongly from the bulk ones [13,25]. Moreover, in view of electronic investigations by averaging techniques (e.g., angle-resolved photoemission spectroscopy), high quality films are a basic requirement.

In order to promote the growth of high quality polar EuO films, we have chosen the Ir(111) surface as substrate. Ir is a noble metal and, therefore, cannot be oxidized under the EuO growth conditions. The high cohesion of Ir implies marginal substrate atom diffusion at the oxide growth temperature and, thus, reduces the probability of mass transport as has been observed for EuO growth on Ni [26]. Hence, together with the low (electronic) corrugation of the dense-packed (111) surface, for Ir(111), the influence of the substrate on EuO growth is minimized prohibiting the formation of complicated surface oxide phases as was observed in the initial growth state of EuO(100) on Ni(100) [26].

The paper is organized as follows: After describing the experimental procedures in Sec. II, in Sec. III, we present the results of our density functional theory (DFT) calculations. Sections IV and V analyze the structure and rotational misalignment of EuO bilayer islands grown by reactive molecular-beam epitaxy using scanning tunneling microscopy (STM) and low-energy electron diffraction (LEED).

*sschumacher@ph2.uni-koeln.de

Section VI is dedicated to work-function measurements and the origin of variations in the apparent height of the EuO islands. Defects and the thermal stability of the EuO(111) bilayer on Ir(111) are analyzed in Secs. VII and VIII. Finally, additional effects on morphology and polarity compensation for larger EuO coverages and our results on the magnetic properties are briefly presented in Secs. IX and X.

II. EXPERIMENT

All experiments were performed in an ultrahigh vacuum system with a base pressure of 3×10^{-11} mbar. As substrate, we used an Ir(111) single crystal, which was initially annealed at 1120 K in a 10^{-6} mbar O_2 atmosphere in order to reduce C impurities. Before each experiment, the sample was cleaned by repeated cycles of sputtering with 2 keV Kr^+ ions between room temperature and 920 K and annealing to 1530 K resulting in clean flat terraces with sizes on the order of 100 nm. Directly before the EuO growth, the substrate was flash annealed to 1530 K and then was cooled to the actual growth temperature (T_{growth}) between 620 and 720 K.

High-purity Eu from Ames Laboratory [27] was evaporated from a water-cooled Knudsen cell. Prolonged degassing of Eu, which usually has a high H_2 content, ensured a background pressure below 1×10^{-10} mbar during growth. Prior to each experiment, a quartz-crystal microbalance was moved to the precise sample growth position for accurately measuring the Eu deposition rate, which is typically on the order of $1 \text{ \AA}/\text{min}$ equivalent to a Eu flux of $f_{\text{Eu}} = 3.5 \times 10^{16} \text{ atoms m}^{-2} \text{ s}^{-1}$.

Molecular O_2 was supplied via a leak valve and was guided through a tube directly to the substrate, which increased the local O_2 pressure at the sample position by a factor of 50 compared to the chamber pressure, resulting in a fast pressure decrease at the end of the growth. We measured the O_2 partial pressure in the chamber by a quadrupole mass spectrometer. The local O_2 pressure was calibrated using adsorption experiments on Ni(100) as described in Ref. [28]. Using kinetic gas theory, the pressure can be expressed as an atom O flux f_O , assuming $f_O = 2f_{O_2}$.

For EuO growth, reactive molecular-beam epitaxy was used, i.e., O_2 and Eu were supplied simultaneously. The amount θ of EuO grown is specified in EuO(111) bilayers (BL), whereby 1 (or 100%) BL is defined as 1 monolayer (ML) of O ions plus 1 ML of Eu ions, each with an atomic surface density of $8.7 \times 10^{18} \text{ atoms m}^{-2}$. This value corresponds to the density of either O or Eu atoms in the (111) planes of bulk EuO. Under O excess, all Eu is expected to react to EuO so that the coverage is calculated by the Eu fluence. On the contrary, under Eu excess, the growth is limited by the amount of O dosed so that we use the O fluence for calculating the coverage. Together, the coverage θ , the flux ratio f_{Eu}/f_O , and the growth temperature T_{growth} fully define the properties of the grown film. We varied the flux ratio f_{Eu}/f_O over a range from 0.85 to 1.7, which does not essentially influence the atomic structure. This is in contrast to the case of EuO growth on a Ni(100) substrate where, already, small changes in the flux ratio cause a variety of surface oxide phases [26].

Imaging was performed with a homebuilt magnetically stabilized variable temperature STM [29] at room temperature if not stated otherwise. Typical parameters are $U_s \approx -0.5 \text{ V}$

for the sample bias and $I \approx 1 \text{ nA}$ for the tunneling current. The images were digitally postprocessed using the WSXM software [30].

LEED measurements were performed using a three grid rearview analyzer. In order to measure lattice constants, the spot positions were determined from images taken by a video camera system directly mounted onto the LEED flange. By averaging over the positions of equivalent spots and calibrating with respect to the substrate spots, we get values for the EuO lattice constants with an error of less than 1%. LEED patterns are displayed with inverted contrast to enhance the visibility of the diffraction spots.

Magneto-optical Kerr effect (MOKE) measurements have been performed *in situ* using a homebuilt setup in longitudinal geometry with a red HeNe laser.

DFT calculations were conducted within the generalized gradient approximation (GGA) of the Perdew-Burke-Ernzerhof type [31] using the Vienna *ab initio* simulation package [32] and the projector augmented-wave basis sets [33,34] with a plane-wave cutoff of 400 eV. The exchange correlation of the Eu $4f$ electrons was taken into account within the GGA + U approach using the Coulomb parameters $U = 7 \text{ eV}$ and $J = 1 \text{ eV}$, which have been shown to be well suited to describe rare-earth systems [35,36].

III. DFT CALCULATIONS

As will be outlined in Sec. IV, for small amounts of EuO grown on Ir(111), we find a EuO(111) bilayer as the only oxide structure. Experimentally, we find a slight orientation scatter between the dense-packed rows of EuO and Ir. Furthermore, the EuO bilayer displays a slightly expanded lattice parameter of 3.67 \AA compared to bulk and, therefore, deviates from a perfect 3:4 registry with Ir(111). As an approximation to the experimental situation accessible to *ab initio* calculations, we use a (3×3) EuO(111) unit cell with an in-plane lattice constant of 3.67 \AA resting on a (4×4) four layer Ir(111) slab with a slightly expanded lattice constant of 2.75 \AA compared to bulk. Fixing the substrate, we relaxed the geometry of the system until the force on every atom was smaller than 0.03 eV \AA^{-1} . The electronic density of states (DOS) has been calculated using the tetrahedron method for Brillouin-zone integration on $5 \times 5 \times 1$ and $10 \times 10 \times 10$ meshes for bilayer EuO on Ir and bulk EuO, respectively.

First, to find out whether O or Eu ions terminate the bilayer to the vacuum, we used both configurations as starting points of the calculations. It was impossible to stabilize a Eu-terminated bilayer on Ir(111), implying O termination, which is also invariably found for other polar bilayer oxides on metal substrates [13,16,37].

Ball models representing the optimized O-terminated EuO(111) bilayer on Ir(111) are shown in Fig. 1. As the most important result, we find an interlayer distance d_1 of only 0.51 \AA . This value is reduced by a factor of 3 compared to the bulk interlayer distance of 1.49 \AA . The finding is stable upon relaxing the first substrate layer as well as upon varying the number of Ir layers in the slab. Furthermore, as a countercheck, we calculated the distance of the (111) planes in bulk EuO and found a value of 1.49 \AA , consistent with the literature value, confirming the reliability of our approach. The reduction in the

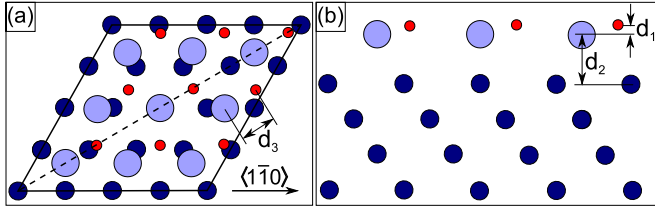


FIG. 1. (Color online) (a) Top view ball model and (b) cut along the dashed line in (a) of the DFT optimization for a EuO(111) bilayer in 3:4 registry with the Ir(111) substrate. Color scheme: Ir: dark blue; Eu: light blue; O: red. $d_1 = 0.51$ Å, $d_2 = 3.07$ Å, and $d_3 = 2.18$ Å denote the thickness of the EuO bilayer, the height of Eu above Ir, and the Eu-O bond length, respectively. The dense-packed $\langle 1\bar{1}0 \rangle$ directions of EuO and Ir are indicated.

bilayer thickness is much stronger than one would expect from the lower coordination in a thin layer which is often thought to cause strengthened and, thereby, shortened bonds [38,39]. We note that this result also implies a strong reduction in the Eu-O bond length d_3 from 2.57 to 2.18 Å.

The driving force for the drastic reduction in the distance between the oppositely charged Eu and O layers is straightforwardly to understand considering a simple capacitor model for the polar bilayer. The difference in electrostatic potential $\Delta\Phi_{BL}$ between the planes, separated by the interlayer distance d_1 and each having a surface charge density σ , is given by

$$\Delta\Phi_{BL} = \sigma \frac{d_1}{\epsilon_0}, \quad (1)$$

where ϵ_0 is the vacuum permittivity. A reduction in the interlayer distance by a factor of 3 from 1.49 Å for the bulk material to 0.51 Å, therefore, reduces $\Delta\Phi_{BL}$ by the same factor and, consequently, the polarity of the film. Indeed, for FeO(111) on Pt(111), a strong reduction in the layer spacing by almost 50% was observed by x-ray photoelectron diffraction [11,40] and has been interpreted to relieve the dipole moment [12].

In order to investigate the coupling between EuO and the Ir substrate, it is instructive to compare the height d_2 of Eu above Ir for the EuO bilayer to the case of Eu adatoms on Ir. We find that $d_2 = 3.07$ Å [see Fig. 1(b)] is substantially larger than the distance between Eu adatoms and Ir, which our DFT calculation finds to be 2.36 Å. The coupling of EuO to Ir is, thus, much weaker than the one of Eu adatoms to Ir. The weak coupling also manifests in the energy required to shift the EuO bilayer laterally out of the minimum position shown in Fig. 1(b). Shifting to a configuration where none of the Eu atoms occupies a high-symmetry site requires less than 5 meV per atom. This energy difference is as small as stacking energy differences for graphene sheets on boron nitride substrates [41], which is dominated by weak van der Waals forces.

To obtain further insight into the bonding and the electronic structure of EuO bilayers on Ir(111), we calculated the total and local DOS and compared them to bulk EuO (see Fig. 2). For bulk EuO, the Fermi level lies inside the band gap as it must be for an insulator; of course, the Ir substrate with adsorbed EuO remains metallic as can be seen from the total DOS. To study the contribution from the EuO bilayer, we projected the total DOS to the local orbitals of Eu and O atoms. Despite the strong structural distortions of the EuO bilayer on Ir, the EuO local

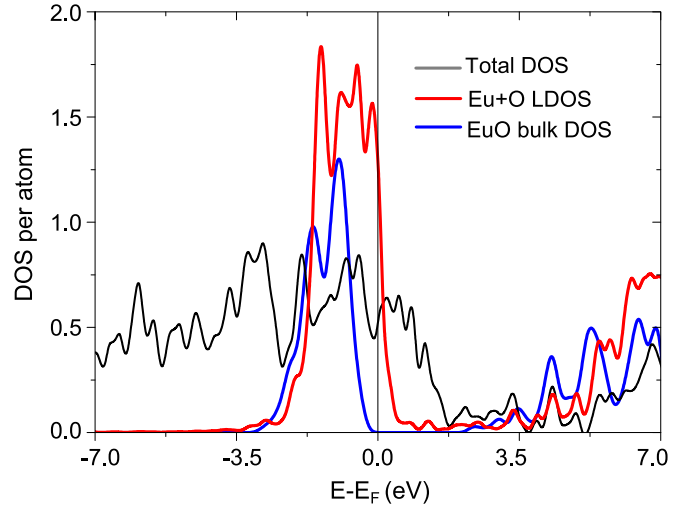


FIG. 2. (Color online) Electronic DOS for a EuO(111) bilayer on Ir(111) and bulk EuO, respectively. The total DOS of EuO on Ir is shown in black, the projected DOS of the EuO bilayer is shown in red, and the DOS of bulk EuO is shown in blue.

DOS is still qualitatively similar to bulk EuO, but in contrast to the bulk, we find that the Fermi level of the EuO bilayer on Ir is located in the valence band of EuO. Thus, electrons are transferred from the bilayer EuO to Ir, indicating a weak ionic bonding of the EuO bilayer to Ir. The charge transfer is energetically favorable as it further reduces the surface electric dipole. Such a surface metallization has also been observed for MgO(111) on Ag(111) [13]. The surface metallization of the EuO bilayer is consistent with our experimental finding that STM imaging can be performed even at very low voltages of several millivolts, which is not expected for an insulating layer.

IV. STRUCTURE

Figure 3 shows a large-scale STM topograph after EuO growth at $T_{\text{growth}} = 720$ K with a flux ratio of $f_{\text{Eu}}/f_{\text{O}} = 1.7$. The Ir terraces labeled with (i)–(iv) are almost fully covered by extended flat O-terminated EuO(111) bilayer islands. The islands on terraces (i), (ii), and (iv) carry a few second layer islands disregarded in the following discussion. Surprisingly, the large bilayer EuO(111) islands are imaged as depressions in the Ir terraces; the decrease in the apparent height is considerable as demonstrated by the line profile taken along the path indicated in the inset of Fig. 3. The step height between the Ir terraces (blue arrow) is 2.2 Å as expected from the Ir crystal structure. However, the step height along the green arrow is 1.5 Å with EuO being lower than Ir. Although the specific value of the height difference depends on the tunneling parameters, under the applied growth conditions, the EuO(111) bilayer was always found to have an apparent *negative* thickness, a puzzle that is resolved by our analysis in Sec. VI. As the O₂ exposure is only sufficient to create, on average, a 23% BL coverage of the Ir(111) substrate, we conclude from the substantially larger coverage in Fig. 3 on considerable local variations due to diffusion during growth (consistent with the large size of the islands). Moreover, this large substrate coverage is consistent with only bilayer and not thicker islands.

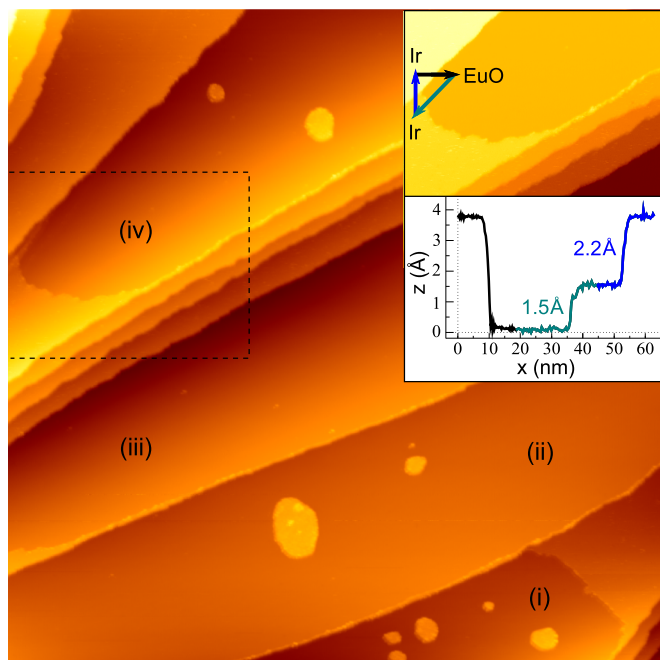


FIG. 3. (Color online) STM topograph of a 23% BL EuO(111) film grown on Ir(111) under $f_{Eu}/f_O = 1.7$ at $T_{growth} = 720$ K (image size 320×320 nm²). Terraces partially covered by EuO are labeled (i)–(iv). Inset: area surrounded by the dotted line with a local plane subtraction applied to align the terraces horizontally. The height profile was taken along the path indicated by differently colored arrows.

The O termination found by our DFT calculations is supported by an interesting morphological feature: The apparent height difference of EuO(111) islands (depressions) and Ir(111) terraces (elevations) enables one to see that the islands grow in contact to ascending step edges and stay away a few nanometers from descending steps, thereby leaving a characteristic rim (compare Fig. 3). The corresponding situation is schematically depicted in Fig. 4. Step edge dipoles are formed on metal surfaces due to smoothening of the electron distribution, which is associated with an excess of negative charge at the step bottom and a lack of negative charge at the step top [42]. The step edge dipole must be assumed to interact with the EuO dipolar layer. A bilayer terminated by negatively charged O ions consistent with DFT explains the observed EuO island repulsion from descending steps and attraction to ascending steps. A terminating Eu layer would cause the opposite effect, which is not observed here.



FIG. 4. (Color online) Schematic side view of EuO(111) bilayer islands at a substrate step edge (light blue: Eu; red: O). The indicated charges correspond to the idealized oxidation states in bulk EuO. The electron density of the substrate (indicated in blue) is smoothed at the step edge, leading to a step edge dipole which attracts the polar EuO bilayer at the ascending step edge and repels it at the descending step edge.

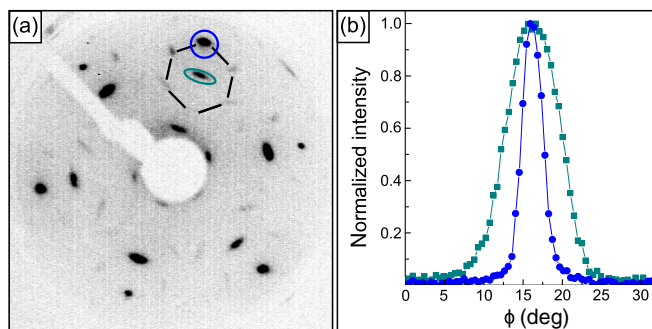


FIG. 5. (Color online) (a) LEED image (76 eV primary electron energy) corresponding to the sample shown in Fig. 3. First-order Ir(111) and EuO(111) spots are exemplarily encircled in blue and green, respectively. Additional superstructure spots are weakly visible and are connected by black lines. (b) Averaged intensity profiles taken in the azimuthal direction over three equivalent spots of Ir (blue dots) and EuO (green squares).

In Fig. 5(a), the LEED image corresponding to the sample presented in Fig. 3 is shown. One of the six first-order Ir substrate spots is marked by a blue circle. Additional intense spots, one of which is encircled in green, are arranged with the same hexagonal symmetry as the substrate reflections but closer to the central spot. They belong to the EuO(111) bilayer with a surface lattice constant of (3.67 ± 0.03) Å and are surrounded by hexagons of weak reflections as indicated by the black lines. A hexagon of spots with identical dimension is also surrounding the central spot (partly hidden by the shadow of the LEED electron source). The weak reflections are located at positions corresponding to vector sums of reciprocal vectors pointing to Ir(111) and EuO(111) spots and may, thus, be interpreted to arise from multiple diffraction. Alternatively, the weak reflections may be assumed to result from the diffraction at the unit cell of a buckled overlayer [43,44].

A closer look reveals that all spots, except the Ir ones, are elongated. In order to quantify the elongation, intensity profiles in the azimuthal direction were taken and were averaged over three equivalent spots. These profiles are presented in Fig. 5(b). The blue dots show the intensity distribution of the Ir(111) first-order spots with a FWHM of $(3.1 \pm 0.3)^\circ$ for the polar angle ϕ . The green squares show the intensity of the first-order EuO(111) bilayer islands. The FWHM of $(7.9 \pm 0.9)^\circ$ is considerably larger, indicating an azimuthal scatter of the EuO(111) bilayer islands around the high-symmetry substrate directions. We note that the magnitude of this scatter sensitively depends on the growth conditions.

Additional insight into the structure of the islands is obtained from atomically resolved STM topographs, such as Fig. 6(a). It displays the hexagonal atomic arrangement of one ion species in the EuO(111) bilayer, presumably the terminating O ions, together with a periodic height modulation of 0.3 Å amplitude, hexagonal symmetry, and a periodicity of approximately three in-plane nearest-neighbor spacings. The corresponding Fourier transform shown as the inset in Fig. 6(a) displays the fundamental periodicity as six spots marked by green circles. The additional superstructure periodicity gives rise to a hexagonal spot arrangement surrounding the fundamental ones (indicated by a black hexagon) and the origin

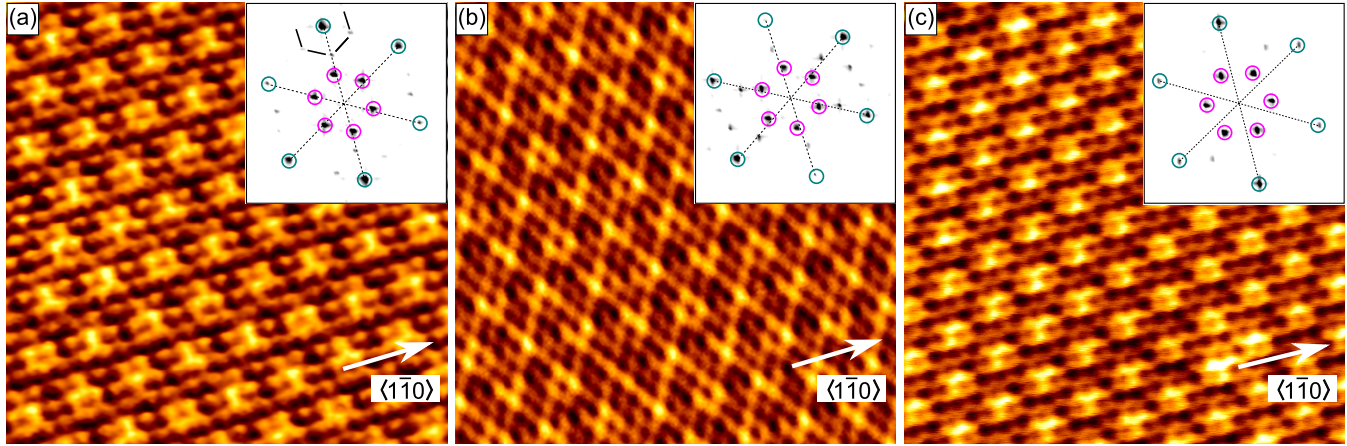


FIG. 6. (Color online) Atomically resolved STM topographs showing EuO bilayer films of different orientations with respect to the substrate. (a) $f_{\text{Eu}}/f_{\text{O}} = 1.7$ and $T_{\text{growth}} = 620$ K. (b) $f_{\text{Eu}}/f_{\text{O}} = 1.7$ and $T_{\text{growth}} = 720$ K. (c) $f_{\text{Eu}}/f_{\text{O}} = 0.85$ and $T_{\text{growth}} = 720$ K. The image size is always 8×8 nm². The insets show the corresponding Fourier transforms. Spots belonging to the atomic lattice are indicated by green circles and are connected by dashed lines, whereas, the spots highlighted in magenta belong to the superstructure. The partial hexagon in (a) connects the higher-order superstructure spots just as in the LEED image of Fig. 5(a). The dense-packed EuO(1 $\bar{1}$ 0) directions are indicated by white arrows.

(magenta circles). Thus, the Fourier transform is similar to the LEED pattern in Fig. 5(a) but without the Ir(111) first-order reflections, which are intense in the LEED pattern due to uncovered substrate areas.

At first sight, it may be surprising that we invariably measure a slight expansion of the EuO(111) lattice parallel to the surface resulting in a lattice parameter of (3.67 ± 0.03) Å, although just a compression of 0.5% would be necessary for a perfect 4:3 epitaxial relation. This deviation of the EuO(111) from an ideal (3×3) superstructure is also visible by close inspection of Fig. 6(a). We interpret the expansion of 0.8% to be (i) enabled by the weak interaction of the EuO(111) bilayer with the Ir(111) substrate and (ii) to be a response to the strongly reduced interlayer distance found by DFT (*Poisson effect*). Such a relation between a reduced interlayer separation and an expanded in-plane lattice parameter has been proven to occur for FeO(111) (1.6% in-plane expansion [12] and 50% reduction in the interlayer spacing [11,40]) and has been proposed for CoO(111) (2.7% in-plane expansion [16]) both on Pt(111). For MgO(111) on Ag(111), up to now, the strongest expansion for the in-plane lattice parameter of a bilayer polar oxide has been observed, amounting to about 10% [13]. Also here, the expansion is likely related to a reduced interlayer distance as the MgO(111) bilayer on Ag(111) has been theoretically predicted to adopt even a planar crystal structure by reducing the layer separation to zero [45].

The omission of an epitaxial relation is in line with the weak interaction of the EuO(111) bilayer with the Ir substrate found by our DFT calculation. Furthermore, it is consistent with the orientation scatter between EuO and Ir apparent in the LEED pattern of Fig. 5, which will be the topic of the next section.

V. ROTATIONAL MISALIGNMENT

Based on our findings above, to a good approximation, we may imagine the EuO(111) islands as a rigid independent lattice, not matched to the substrate but with preferred orientation. Consequently, the EuO(111) lattice is not commensurate to the

substrate lattice but forms a moiré with it. Figures 6(a)–6(c) display EuO(111) bilayer islands with different degrees of rotational misalignment. As can be straightforwardly deduced from the topographs or their Fourier transforms, the superstructures are rotated with respect to the dense-packed EuO(111) rows by angles $\phi_{\text{EuO},s} = (3.5 \pm 0.5)^\circ$ in Fig. 6(a), $\phi_{\text{EuO},s} = (5 \pm 1)^\circ$ in Fig. 6(b), and $\phi_{\text{EuO},s} = (19 \pm 2)^\circ$ in Fig. 6(c). We note that the latter is close to a $(\sqrt{7} \times \sqrt{7})R19.1^\circ$ superstructure, but a change in the local atomic arrangement at the moiré maxima over the extension of the topograph also indicates the incommensurability between EuO(111) and Ir(111) in this case.

Formally, the moiré reciprocal lattice vector \vec{k}_s is generated by the vector difference of the reciprocal lattice vectors \vec{k}_{Ir} of Ir and \vec{k}_{EuO} of EuO: $\vec{k}_s = \vec{k}_{\text{Ir}} - \vec{k}_{\text{EuO}}$. If the atomic lattices include an angle $\phi_{\text{EuO},\text{Ir}}$, the superstructure is rotated by an angle $\phi_{\text{EuO},s}$ with respect to the EuO lattice as shown in the schematic in Fig. 7. Both angles are connected by the relation,

$$\phi_{\text{EuO},s} = \tan^{-1} \left(\frac{\sin \phi_{\text{EuO},\text{Ir}}}{\frac{k_{\text{Ir}}}{k_{\text{EuO}}} - \cos \phi_{\text{EuO},\text{Ir}}} \right) + \phi_{\text{EuO},\text{Ir}} \quad (2)$$

$$\approx \frac{k_{\text{Ir}}}{k_{\text{Ir}} - k_{\text{EuO}}} \phi_{\text{EuO},\text{Ir}} \quad \text{for } \phi_{\text{EuO},\text{Ir}} \ll 1, \quad (3)$$

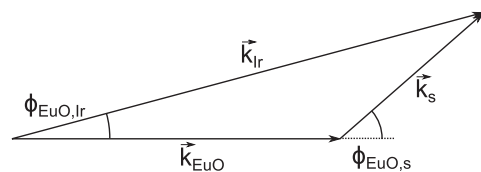


FIG. 7. Superposing the lattices of EuO and Ir with reciprocal lattice vectors \vec{k}_{EuO} and \vec{k}_{Ir} under an angle $\phi_{\text{EuO},\text{Ir}}$ results in a superstructure with reciprocal lattice vector $\vec{k}_s = \vec{k}_{\text{Ir}} - \vec{k}_{\text{EuO}}$, which is rotated by $\phi_{\text{EuO},s}$ with respect to \vec{k}_{EuO} .

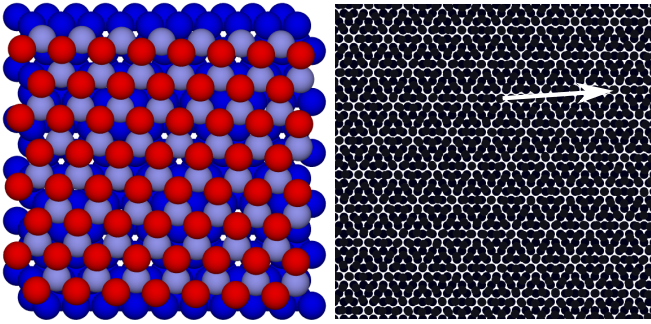


FIG. 8. (Color online) Top view ball model for a EuO(111) bilayer island on Ir(111) rotationally misaligned by $\phi_{\text{EuO,Ir}} = 1.3^\circ$ as in the topograph of Fig. 6(b). The experimentally determined lattice parameter $a_{\text{EuO}} = 3.67 \text{ \AA}$ is used for EuO(111). Color scheme: Ir: dark blue; Eu: light blue; O: red. In the right part, the resulting moiré is emphasized by overlaying the EuO and Ir lattices as black dots. The white arrow shows the dense-packed direction of the moiré superstructure.

whereby Eq. (3) is an approximation for small angles. By inserting the bulk value of 0.368 \AA^{-1} for k_{Ir} and $k_{\text{EuO}} = 0.272 \text{ \AA}^{-1}$ from the LEED measurement in the equations above, we obtain a rotation of the EuO lattice with respect to the Ir one of $\phi_{\text{EuO,Ir}} = (0.9 \pm 0.2)^\circ$ for Fig. 6(a), $\phi_{\text{EuO,Ir}} = (1.3 \pm 0.3)^\circ$ for Fig. 6(b), and $\phi_{\text{EuO,Ir}} = (5.2 \pm 0.5)^\circ$ for Fig. 6(c). By comparing these values of $\phi_{\text{EuO,Ir}}$ to the corresponding $\phi_{\text{EuO,s}}$ ones, it is obvious that the moiré amplifies the misalignment of the EuO and Ir lattices. In the small-angle approximation of Eq. (3), this amplification factor is $k_{\text{Ir}}/(k_{\text{Ir}} - k_{\text{EuO}}) \approx 3.84$.

The situation is visualized for the example of Fig. 6(b) in the ball models of Fig. 8. In the ball model to the left, the EuO(111) bilayer is superimposed to the Ir(111) substrate with the measured lattice parameter of $(3.67 \pm 0.03) \text{ \AA}$ and the angle $\phi_{\text{EuO,Ir}} = (1.3 \pm 0.3)^\circ$ as derived above from the measured $\phi_{\text{EuO,s}}$. In order to illustrate the resulting moiré in the right part of Fig. 8, both the EuO and the Ir lattices are formed by black dots resulting in an enhanced contrast. The moiré and the magnification of the rotation of the underlying lattices are well visible.

Moiré structures with similar orientation scatters are also known for other thin polar oxide films on metal substrates as, e.g., FeO(111) on Pt(111) [37,43,46]. They occur for incommensurate layers with a weak and unspecific interaction as found in our case. Such a rotational epitaxy has been theoretically analyzed in the past for weakly interacting layers [47,48] and has been experimentally observed, e.g., for incommensurate physisorbed noble gas monolayers on graphite [49].

VI. APPARENT HEIGHT AND WORK FUNCTION

As already discussed in Sec. IV, the EuO(111) bilayer islands appear as depressions in the surrounding terraces under Eu-rich growth conditions (compare Fig. 3). The reduction in apparent height is substantial as we calculate a geometric height of 3.58 \AA for the EuO(111) bilayer on Ir(111) (compare Sec. III). In this section, we will demonstrate that the apparent height of the EuO(111) bilayer islands changes with the growth

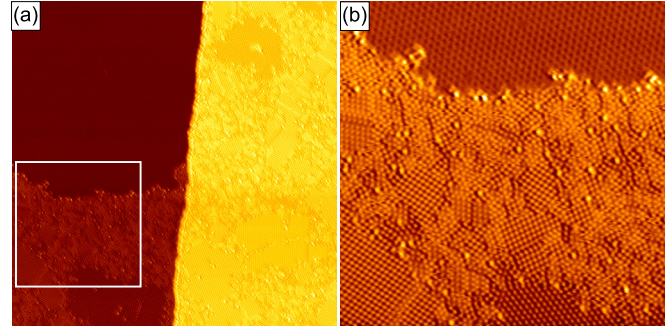


FIG. 9. (Color online) (a) STM topograph taken at 35 K of a partial EuO(111) bilayer grown under 70% Eu excess ($130 \times 130 \text{ nm}^2$). The upper left corner consists of EuO(111), whereas, the rest of the image is Ir(111) covered by Eu adatom phases of different densities. (b) Zoom into the area marked by a white square in (a) ($50 \times 50 \text{ nm}^2$).

conditions. Depending on whether they are Eu or O rich, either Eu or O is adsorbed to the bare Ir(111) terraces next to the EuO(111) bilayer islands. This adsorbate layer does not only affect the *topographic* height difference between the EuO(111) islands and their surroundings, but also affects the tunneling process via its influence on the work function.

Figure 9 displays an STM topograph of EuO grown under the same conditions as used for the topograph in Fig. 3 ($f_{\text{Eu}}/f_{\text{O}} = 1.7$ and $T_{\text{growth}} = 720 \text{ K}$) but imaged at 35 K instead of room temperature. The lower substrate terrace in the upper left corner of Fig. 9(a) is partially covered by EuO(111), whereas, on the remaining terrace, we find a complex variety of incommensurable Eu adatom phases better visible in the zoom of Fig. 9(b). Areas with higher adatom density appear brighter than areas with lower density. The average nearest-neighbor distance of the adatoms is $(8.0 \pm 0.5) \text{ \AA}$. Assuming an ideal hexagonal arrangement, this distance corresponds to a coverage of 11.5% ML with respect to Ir(111). Upon depositing 23% BL EuO(111) with a flux ratio of $f_{\text{Eu}}/f_{\text{O}} = 1.7$, the Eu excess is expected to cover 12% of the remaining Ir(111) surface atoms in excellent agreement with our observation. The excess Eu is distributed as single adatoms rather than islands on Ir(111) since the positively charged ions are subject to Coulomb repulsion [50]. At 300 K imaging temperature, as used for Fig. 3, the Eu adatoms are highly mobile and form a structureless background, at first glance, indistinguishable from a bare Ir(111) terrace. The adsorbed Eu adatom phase thereby creates, in STM, an additional topographic height on the Ir(111) terrace that contributes to the impression of an apparent negative height of the EuO(111) bilayer islands.

In order to confirm the influence of the dilute Eu adatom phase on the apparent height, we exposed the sample to additional O_2 in order to remove the mobile Eu adatoms. The corresponding experiment is shown in Fig. 10. The film in Fig. 10(a) was grown under Eu-rich conditions ($f_{\text{Eu}}/f_{\text{O}} = 1.7$). The schematic in Fig. 10(g) along the black line illustrates the morphology of the sample. On the lower Ir terrace, we find a triangular area not covered by EuO, whereas, on the upper terrace, a rim adjacent to the step edge is uncovered. In the initial stage, EuO appears 0.4 \AA lower than the surroundings as expected under these growth conditions.

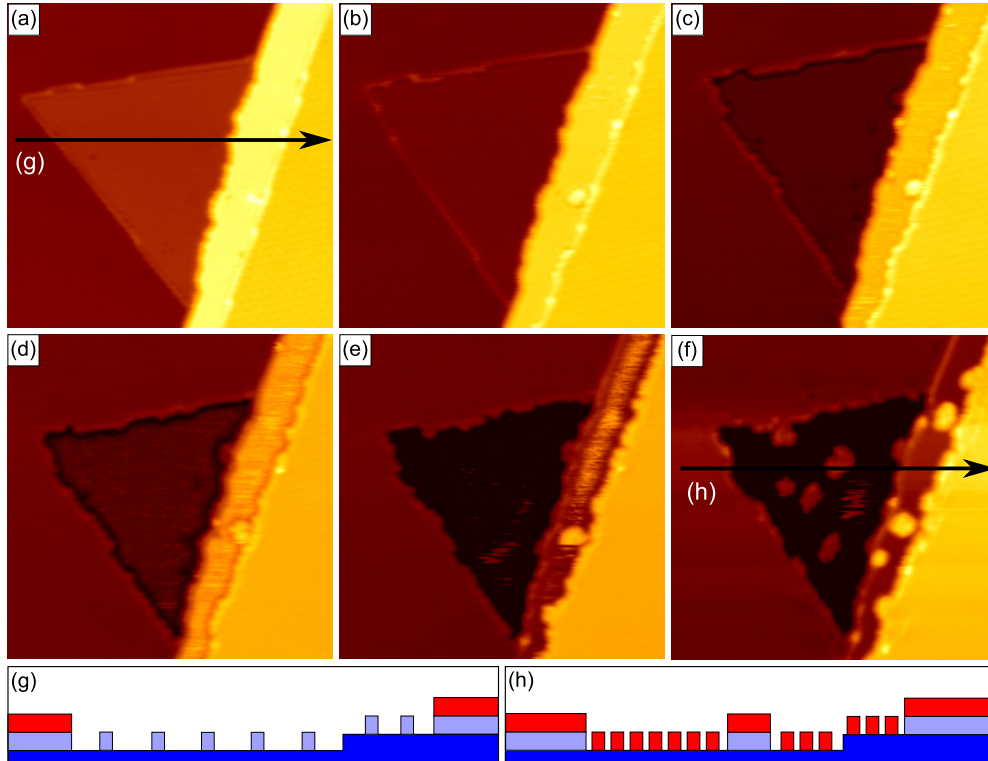


FIG. 10. (Color online) (a)–(f) STM topographs of a partial EuO(111) film grown under Eu excess (image size always $40 \times 40 \text{ nm}^2$). Brightness and contrast are adjusted for the EuO layers on the lower and upper Ir terraces. During tunneling, the sample was exposed to $1 \times 10^{-8} \text{ mbar O}_2$ at 300 K. The O_2 exposure (given in langmuirs) increases from (a) 0 L via (b) 2 L, (c) 4 L, (d) 6 L, and (e) 8 L to (f) 10 L. The apparent height of Ir continuously decreases from $+0.4 \text{ \AA}$ to -1.8 \AA with respect to the EuO level. (g) and (h) show schematics taken along the lines in (a) and (f), respectively. Color scheme: Ir: dark blue; Eu: light blue; O: red.

During exposure of the sample to a total amount of 10 L O_2 at 300 K, the sequence of images shown in Figs. 10(b)–10(f) was taken. Upon O_2 exposure, there is no sign of adsorbed O or structural changes in the EuO islands. The invariable appearance of the EuO islands confirms our finding that the bilayer is terminated by a layer of O ions because a topmost Eu layer would be expected to react with the supplied O.

In contrast, upon O_2 dosing, the apparent height of the Ir terrace substantially decreases such that it appears 1.8 \AA lower than the EuO(111) bilayer islands after an exposure to 10 L O_2 . At the same time, the noise level on the Ir terrace initially increases, reaches a maximum in Figs. 10(d) and 10(e), and eventually vanishes in Fig. 10(f), whereas, new EuO(111) islands have formed at the preexisting EuO edges and on bare Ir(111).

We explain the observations as follows: Upon O_2 exposure, O adsorbs and dissociates on the surface reacting with the Eu adatoms to EuO. The mobile EuO species incorporate into existing EuO island edges. Due to the increasing amount of mobile O, the noise level increases. When a certain O amount is reached, O forms a dense saturation layer and loses its mobility, resulting in the disappearance of the noise. EuO species created in this late state of oxidation have a reduced mobility due to the O adlayer and, thus, nucleate as new small islands. This corresponds to the situation shown in Fig. 10(f) and is sketched in the corresponding line profile in Fig. 10(h).

Knowing that at room temperature the apparent height of the EuO(111) bilayer islands must be referenced to the level of the

adsorbate layer and not the bare Ir(111) terrace certainly helps to understand why the islands are imaged initially as depressions with 0.4 \AA depth. However, the change in the apparent EuO(111) bilayer island height from -0.4 \AA to $+1.8 \text{ \AA}$ cannot be explained by geometric heights—the level of the Eu and O adsorbate layers is similar. This effect results from the change in the work function in the areas free of EuO(111) caused by the oxidation-induced replacement of the Eu adatom phase through an O adsorbate layer. Indeed, within the Wentzel-Kramers-Brillouin approximation, the tunneling current I through a one-dimensional barrier of width z is given by

$$I(z) \propto \exp(-k\sqrt{\bar{\Phi}}z), \quad (4)$$

with the constant $k = 1.025 \text{ eV}^{-1/2} \text{ \AA}^{-1}$ and the apparent barrier height $\bar{\Phi}$, which is proportional to the work function [51]. Thus, the work function directly influences the apparent height in the constant current mode.

A suitable technique to measure work-function differences is $I(z)$ spectroscopy. By measuring the decay of the tunneling current with increasing tip distance above sample positions A and B, one can determine the apparent barrier height difference $\Delta\bar{\Phi} = \bar{\Phi}_A - \bar{\Phi}_B$. For a simple trapezoidal barrier, the work-function difference $\Delta\Phi$ is just twice the apparent barrier height difference $\Delta\bar{\Phi}$ [50].

Figure 11 shows the distance-dependent tunneling current decay in logarithmic scale. All measurements were performed using a bias voltage of $U_s = 0.5 \text{ V}$ and a stabilization current

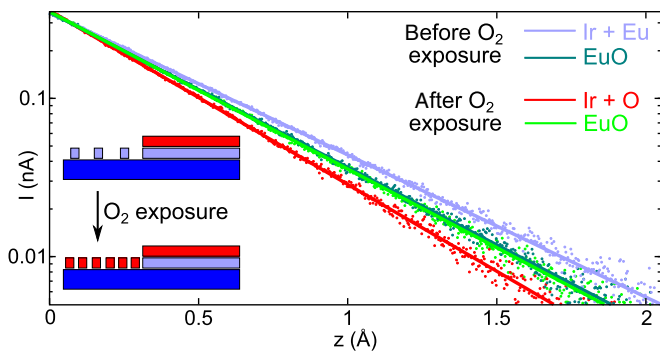


FIG. 11. (Color online) $I(z)$ measurements on Eu-covered Ir (light blue) and EuO (dark green) measured on a 23% BL EuO(111) film grown under $f_{\text{Eu}}/f_{\text{O}} = 1.7$ at $T_{\text{growth}} = 720$ K. The additional data for O-covered Ir (red) and EuO (light green) are taken on the same sample after 10 L O_2 exposure. The solid lines are exponential fits to the data points.

of $I_0 = 0.35$ nA. After opening the feedback loop, the tip was retracted by 3 \AA within 0.5 s while a small z piezodrift was actively compensated. The data were averaged over several measurements and were fitted with an exponential function to yield values for the apparent barrier height.

The first set of measurements was performed on the surface shown in Fig. 10(a) before O_2 exposure. For the EuO(111) bilayer, we obtain an apparent barrier height of $\bar{\Phi}_{\text{EuO}} = (4.89 \pm 0.02)$ eV (dark green) and for the Ir(111) substrate covered with a Eu adatom phase $\bar{\Phi}_{\text{Ir+Eu}} = (4.09 \pm 0.02)$ eV. This results in a work-function difference of $\Delta\Phi = (1.60 \pm 0.06)$ eV with the work function of EuO(111) being higher than the one of Eu-covered Ir(111). By measuring Gundlach oscillations (see Supplemental Material [52]), we get $\Delta\Phi = (1.77 \pm 0.02)$ eV in good agreement with the $I(z)$ result. The deviation of the values obtained by the two entirely different methods also provides an estimate for the magnitude of the systematic errors involved in our approach.

After 10 L O_2 exposure corresponding to the situation in Fig. 10(f), the apparent barrier height for the EuO(111) bilayer stays almost unchanged at $\bar{\Phi}_{\text{EuO}} = (5.07 \pm 0.03)$ eV (light green). The slight difference of 4% most likely results from minor tip changes during gas exposure. In contrast, we observe a strong increase in the apparent barrier height for the Ir(111) terrace to $\bar{\Phi}_{\text{Ir+O}} = (6.13 \pm 0.04)$ eV as the terraces are now covered by O adsorbates instead of Eu adatoms. Hence, the work-function difference is $\Delta\Phi = (2.14 \pm 0.10)$ eV with the work function of the EuO(111) bilayer being lower than the one of O-covered Ir(111).

In order to get quantitative estimates for the work functions of the different structures, we use the O-saturated Ir(111) surface as a reference. As known from literature, O adsorbed on an Ir(111) surface gives rise to a work-function increase of 0.56 eV at saturation coverage [53]. Combining this with the work function for pristine Ir(111) ($\Phi_{\text{Ir}} = 5.76$ eV [54]), we expect a value of $\Phi_{\text{Ir+O}} = 6.32$ eV. On the basis of this reference, we estimate the work function of Eu-covered Ir(111) to be $\Phi_{\text{Ir+Eu}} = (2.58 \pm 0.12)$ eV, i.e., about 3.8 eV lower than the one of O-covered Ir(111). This large difference explains the considerable change in apparent height of the Eu(111) bilayer islands with respect to their surroundings upon O_2 exposure.

The low work function of Eu-covered Ir(111) is close to the value for bulk Eu of 2.5 eV [55] showing that it is mainly determined by the dilute Eu adatom phase.

Again, using the O-covered Ir(111) surface as a reference, for the EuO(111) bilayer islands, we obtain $\Phi_{\text{EuO}} = (4.18 \pm 0.10)$ eV. Compared to EuO(100) with a work function reported to be only 0.6 eV [56,57], this value is remarkably high. Based on the expectation of a substantial dipole moment for the polar orientation of the oxide surface, one might have expected an even larger work function. However, as pointed out in Sec. III and discussed in relation with Fig. 2, the metallicity of the bilayer implies a charge transfer to the electronegative substrate that tends to reduce the total surface dipole and, thus, the work function. In addition, the compression of the metal electron density tail by the oxide film was pointed out to be an additional factor that tends to lower the work function [15,58]. Whereas local variations for the surface potential in a polar oxide film as well as local barrier heights were already reported a number of times [15,59,60], here we report on the experimental estimates for absolute values of the work function for a polar oxide film.

Using DFT, we calculated the work function of a bilayer EuO(111) on Ir(111). Based on the optimized structures (compare Sec. III) and using a vacuum length of about 50 \AA and the periodic images of the slabs, we carried out a self-consistent calculation to obtain the Fermi energy E_{F} and the vacuum energy E_{V} ; the work function Φ is then equal to $E_{\text{V}} - E_{\text{F}}$. First, we determined the work function of bare Ir(111) and found a value of 5.52 eV. The slight deviation from the literature value of 5.76 eV gives the systematic error of our approach. Next, we calculated the work function for 12.5% ML Eu on Ir(111) employing a dipole correction. The Eu coverage is close to the experimentally observed one of 11.5% ML with respect to Ir(111). The result of $\Phi_{\text{Ir+Eu}} = 2.51$ eV is in excellent agreement with the 2.58 eV obtained from experiment. Finally, for the EuO bilayer on Ir(111), we find a work function of $\Phi_{\text{EuO}} = 6.06$ eV.

Consistent with the experiment, this value is substantially higher than the EuO(100) work function but considerably deviates from the experimental result of about 4.2 eV. We cannot offer a sound explanation for this deviation. Although the experimental and calculated work functions agree rather well for Eu-covered Ir(111) ($\Phi_{\text{Ir+Eu}}$) and a number of cases investigated by us in the past [50,61], certainly the assumption of a simple trapezoidal tunneling barrier is a severe simplification and might give rise to a substantial error for the experimental estimate under specific conditions. On the other hand, our experimental finding that the metal-supported polar oxide bilayer has a lower work function than the bare substrate is consistent with results obtained for MgO(111) on Au(111) [60].

VII. DEFECTS

In the previous STM images different types of defects in the EuO layer were already visible, which we now analyze in more detail. In Fig. 12(a), arrows highlight a few of the many defects that appear as missing superstructure protrusions. They have a much higher areal density for $T_{\text{growth}} = 620$ K than for $T_{\text{growth}} = 720$ K. In the inset of Fig. 12(a), two adjacent defects are enclosed by hexagons. The atomic rows unaffectedly run

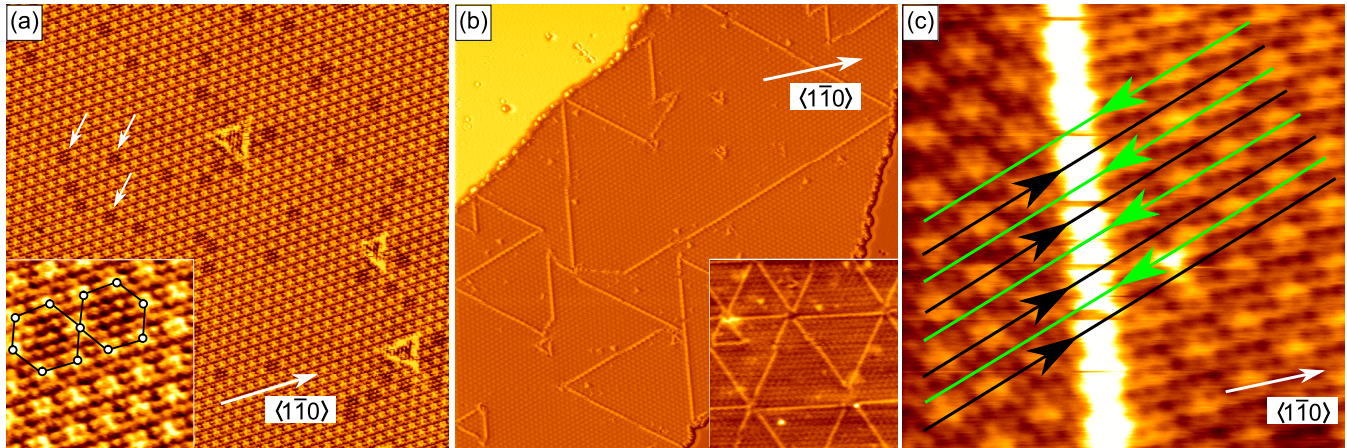


FIG. 12. (Color online) STM topographs showing different types of defects in EuO bilayer films. (a) $f_{\text{Eu}}/f_{\text{O}} = 1.7$ and $T_{\text{growth}} = 620$ K (37×37 nm²). Inset: point defects (indicated by arrows in the large-scale image) appear as missing superstructure protrusions which are indicated by the white dots (5×5 nm²). (b) $f_{\text{Eu}}/f_{\text{O}} = 0.85$ and $T_{\text{growth}} = 720$ K (79×79 nm²). Inset: Zoom into a EuO island (29×29 nm²). (c) Same growth conditions as for (b). Green and black lines indicate dense-packed superstructure rows on the right- and left-hand sides of the bright stripe, respectively (8×8 nm²). The EuO $\langle 1\bar{1}0 \rangle$ directions are indicated.

through the defects, i.e., there seem to be no missing or shifted atoms. Therefore, such superstructure defects likely mark missing atoms below the top layer which would be Eu vacancies.

In Fig. 12(b), bright stripe defects are visible. They follow the directions given by the superstructure and often form triangular networks, which are especially well visible in the inset of Fig. 12(b). The smallest version of such a triangle is also present in Fig. 12(a). The bright stripes are due to antiphase domain boundaries. When two EuO(111) islands grow together, it is improbable that their superstructures fit together as there are different translational domains due to the large size of the moiré unit cell. In such a case, a line-type defect is expected at which a registry shift in the superstructures occurs.

Evidence for this interpretation is given in Fig. 12(c), which shows such a bright stripe with the atomic and superstructure lattices well resolved on both sides. The black lines lie on top of the dense-packed rows of the bright superstructure protrusions on the left-hand side of the stripe, whereas, the green lines follow the superstructure rows on the right-hand side of the bright stripe. The lines are shifted with respect to each other on both sides of the stripe, thereby confirming that the stripes are due to antiphase domain boundaries. Similar line defects forming triangular structures also appear for thin layers of FeO(111) [62] as well as CoO(111) [16] and have been interpreted as O vacancies forming dislocation loops. Here, this can be ruled out as the defects do not change upon O₂ exposure and are mostly observed under O-rich growth conditions. We interpret the latter observation as follows: The higher O chemical potential apparently drives the growth kinetics towards formation of smaller domains by reducing the mobility of the initial oxide species. A similar effect has been previously observed for FeO(111) nanoislands on Pt(111) [63].

VIII. TEMPERATURE STABILITY

Although the term *polar surface* bears the connotation of instability, we show here that the EuO(111) bilayer on

Ir(111) is a surprisingly stable two-dimensional material. As demonstrated by the LEED pattern in Fig. 13(a), annealing of the EuO(111) bilayer up to 1420 K does not show any structural degradation of the material. On the contrary, the rotational misalignment of the film and the diffuse background are considerably lowered. Both effects can be attributed to annealing of defects in the film and the ensuing increase in the domain size. The lattice constant of (3.67 ± 0.03) Å is still slightly expanded compared to the bulk value and, therefore, prohibits an ideal epitaxial 3:4 relation of EuO(111) and Ir(111). The STM image in Fig. 13(b), taken after annealing to 1420 K, confirms the excellent film quality and the reduced defect density. Although the island size has substantially increased, the characteristic rim of uncovered Ir close to the descending step edge is still present. As we consider the rim to be an effect of the bilayer dipole, we conclude that polarity in the film also remains after annealing.

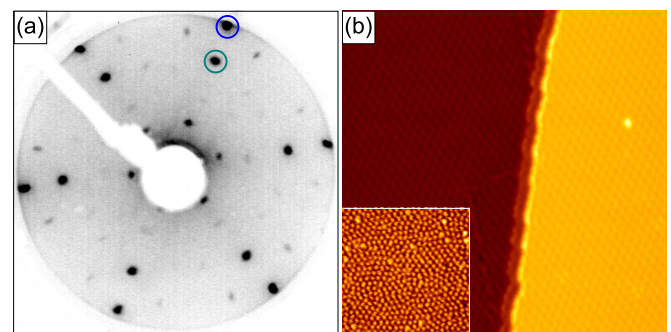


FIG. 13. (Color online) (a) LEED image (54 eV primary electron energy) of a EuO film (23% BL, $f_{\text{Eu}}/f_{\text{O}} = 1.7$ and $T_{\text{growth}} = 720$ K) after annealing to 1420 K for 60 s. Ir and EuO first-order spots are highlighted in blue and green, respectively. (b) Corresponding STM topograph (40×40 nm²). The whole image is covered by a closed EuO film except for the small rim close to the descending substrate step edge. The inset (30×30 nm²) shows the dilute Eu adatom phase on Ir at 35 K.

As visible on the upper terrace of Fig. 13(b), upon annealing to 1420 K, the apparent height of the EuO islands with respect to the substrate has changed as they now appear higher than the surrounding ones. Once more, we had a look at the Eu adatoms on Ir(111) at 35 K and found that the phase had been diluted upon annealing to 1420 K, either through reevaporation to the vacuum or through diffusion into the bulk. Compared to the situation before annealing, the Eu nearest-neighbor distance increased from (8.0 ± 0.5) Å to (13.0 ± 0.5) Å corresponding to a coverage decrease from 11.5% to 4.4%. The reduced adatom density gives rise to a higher work function and, therefore, to an increase in the apparent EuO height with respect to the surroundings. Our findings here are consistent with the observation in Fig. 9 that the apparent height depends on the adatom density. We note that, upon annealing to even higher temperatures, the spots belonging to EuO become gradually weaker but are still visible until 1520 K and eventually vanish at 1570 K.

EuO bulk crystals have a high formation enthalpy of 5.85 eV/atom [64] attesting a strong Eu-to-O binding. In contrast, we found an unspecific and weak interaction of the oxide film with the substrate. Therefore, one might have expected a phase transformation to the more stable Eu_2O_3 or a transformation of the two-dimensional material to three-dimensional crystallites. The absence of such structural and morphological transformations indicates a deep energetic minimum of the EuO(111) bilayer on Ir(111). Its robustness makes it an interesting candidate for the toolbox of surface engineering with two-dimensional materials.

IX. INFLUENCE OF THE EU EXCESS

Under Eu-rich growth conditions, in the previous sections, we have seen that surplus Eu remains on the Ir surface during EuO growth. Increasing the deposited amount while maintaining the Eu-rich growth conditions will cause a larger surface fraction to be covered by EuO(111) bilayer islands. The question arises, whether the increasing Eu excess is still accommodated on the decreasing area of Ir(111) terraces as a Eu adatom phase or squeezed onto the EuO(111) bilayer islands. In order to answer this question, a larger coverage of $\theta = 51\%$ BL was deposited at $T_{\text{growth}} = 720$ K with a flux ratio of $f_{\text{Eu}}/f_{\text{O}} = 1.7$. In the corresponding STM topograph in Fig. 14(a), the surface is fully covered by two different structures: (i) A flat surface labeled as Eu with hexagonal lattice symmetry as shown in Fig. 14(b). (ii) A structure labeled as EuO(111) with a rough appearance consisting of triangularly shaped objects as can be seen from the zoomed images in Figs. 14(c) and 14(d).

We interpret the structure labeled as Eu in Fig. 14(a) to arise from Eu adsorbed to Ir(111) terraces. Due to the higher coverage, it forms a dense Eu layer instead of a dilute adatom phase. In LEED (not shown here), we find spots in a hexagonal arrangement corresponding to a lattice constant of 4.2 Å. This value is just in between the two Eu-Eu distances for an (110) plane of bulk Eu, which is quasihexagonal with atomic distances of 3.07 and 4.58 Å along and across the $\langle 001 \rangle$ chains, respectively. The pattern visible in Fig. 14(b) has a nearest-neighbor distance of about 10 Å and, therefore, has to be a superstructure. Consistent with our assignment as

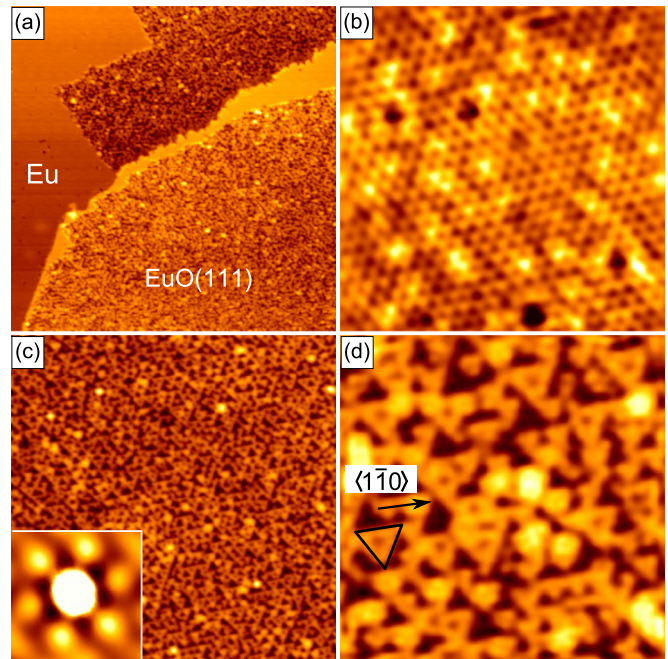


FIG. 14. (Color online) STM topographs showing a EuO film with 51% BL nominal coverage grown under $f_{\text{Eu}}/f_{\text{O}} = 1.7$ at $T_{\text{growth}} = 720$ K. (a) Overview over the occurring structures (160×160 nm²). (b) Eu structure of (a) (20×20 nm²). (c) EuO(111) structure of (a) (70×70 nm²). Inset: Self-correlation. (d) Same as (c) (20×20 nm²). One of the most common triangles with edges parallel to the EuO $\langle 1\bar{1}0 \rangle$ directions is indicated.

the Eu layer, the structure appears defective, which we attribute to the high reactivity of metallic Eu.

Next, we address the structure labeled as EuO(111) in Fig. 14(a). From the higher-resolved topographs in Figs. 14(c) and 14(d), one can see that it consists of either triangular depressions or protrusions on an otherwise flat surface. The edges of the triangles are aligned with the EuO $\langle 1\bar{1}0 \rangle$ directions. In the self-correlation of Fig. 14(c), which is shown in the corresponding inset, a characteristic hexagonal order with a separation of about 2.2 nm was found, but as the size of the triangles is obviously not homogeneous, there exists no long-range order. The 2.2 nm are slightly more than the length of the largest triangles, one of which is indicated in Fig. 14(d). These show depressions at their centers and give the impression that they consist of three smaller triangles at their corners. Thus, the large triangles probably appear when three small triangles have formed in the closest possible distance to each other. Hence, the 2.2 nm should be the shortest repetition distance of the small triangles. Due to a lack of resolution in STM imaging, further details of this structure cannot be determined.

Triangular motifs as observed here are often found in surface reconstructions which occur to avoid the high electrostatic potential of polar surfaces. Especially, the appearance of the polar (0001)-Zn surface of ZnO in STM is qualitatively very similar [65]. Thus, we tentatively attribute the structure to consist of a EuO(111) bilayer where a reconstructed partial third Eu layer has grown on top. The material for the partial

layer stems from Eu that could not be accommodated anymore in the dense Eu layer binding to the Ir(111) substrate.

Further evidence for the compensating effect of the Eu adlayer comes from the structure of the polar bilayer: LEED displays a EuO(111) phase with a lattice parameter of 3.62 Å, i.e., there is no further need for an expanded lattice constant. With the reduced lattice parameter, the EuO(111) perfectly fits in a 3:4 registry with the Ir(111) substrate resulting in a lack of rotational misalignment.

X. MAGNETIC PROPERTIES

Since EuO is a ferromagnetic semiconductor, it is of interest to explore whether the EuO(111) bilayer displays magnetic order at accessible temperatures. Whereas, Kondo lattice model calculations predict a substantially decreased T_C for ultrathin EuO films with respect to the bulk value of 69 K [66], recently, EuO(100) films with thicknesses of a few nanometers were demonstrated to even display an enhanced T_C [67].

Reactive molecular-beam epitaxy under Eu-rich growth conditions prohibits the completion of the EuO(111) bilayer without a reconstructed third layer. Therefore, a monolayer of Eu was deposited onto Ir(111) at room temperature and was reacted to EuO(111) by subsequent O₂ exposure and annealing to 720 K. LEED shows an intense EuO(111) diffraction pattern. Since the polar bilayer is slightly denser than the saturated Eu layer, the surface is covered by about 90% BL EuO(111), i.e., an almost complete polar bilayer was realized.

In order to explore the magnetic properties of this layer, we conducted MOKE measurements. Within the accessible resolution of 10 μrad in the Kerr angle, no ferromagnetic behavior could be detected down to a sample temperature of 45 K. Certainly, our observation does not exclude a coupling of the bilayer at even lower temperatures.

XI. CONCLUSIONS

High quality bilayer films of polar EuO(111) can be grown on Ir(111), either through reactive molecular-beam epitaxy over a broad flux ratio regime with $0.85 \leq f_{\text{Eu}}/f_{\text{O}} \leq 1.7$ and in a temperature range from 620 to 720 K or through Eu deposition and subsequent annealing to 720 K in molecular O₂. The EuO(111) bilayer is thermally highly stable up to 1420 K.

Using DFT, we find the EuO(111) bilayer is in contact with the Ir(111) substrate with its Eu layer and exposes its O layer to the vacuum. This theoretical result is backed up by the absence of structural changes upon *in vivo* exposure to O₂ as expected only for O termination.

EuO(111) bilayer islands do not obey a strict epitaxial relation with respect to the substrate, although just a compression of 0.5% would result in 3:4 registry along the dense-packed rows of Ir(111) and EuO(111). Instead, they grow with an in-plane lattice parameter expansion of about 0.8% and in rotational epitaxy with a scatter of up to 5° between the dense-packed rows of substrate and bilayer. The rotational misalignment gives rise to a variety of moiré patterns and signifies a weak interaction between substrate and bilayer, consistent with the large spacing between the Ir surface and

the Eu atoms in the bilayer as found in our DFT calculations. The orientation scatter between substrate and bilayer islands sensitively depends on the film preparation conditions and reduces upon high-temperature annealing.

The in-plane lattice parameter expansion was identified as a consequence of the Poisson effect, namely, to result from a drastic contraction of the bilayer thickness from 1.49 Å in bulk EuO to 0.51 Å on Ir(111). This substantial reduction in the separation between the oppositely charged Eu and O layers must be considered as a prime mechanism to reduce the electrostatic potential within the film. An analysis of the projected DOS of the EuO(111) bilayer on Ir(111) shows that the bilayer is metallic. The associated electron transfer from the bilayer to the substrate provides an additional contribution to reduce the film polarity. The metallicity of the bilayer is consistent with our ability to image the EuO(111) bilayer on Ir(111) by STM in atomic resolution and down to voltages in the millivolt range. The residual dipole moment of the EuO(111) bilayer implies an electrostatic interaction with the step dipoles of the Ir(111) substrate. This interaction causes the EuO(111) bilayer islands to keep their distance from descending steps while they attach to ascending ones. For large coverages under Eu-rich growth conditions, an additional mechanism of polarity reduction was found: Eu is squeezed onto the EuO(111) bilayer islands where it creates a partial adlayer consisting of triangular patches of well-defined size. This partial Eu layer adsorbed to EuO(111) lifts the in-plane lattice parameter reduction (and presumably the bilayer contraction), brings the islands into perfect epitaxy with the substrate, and lifts the rotational misalignment.

In reactive molecular-beam epitaxy, we find that depending on whether the growth conditions are Eu or O rich, either atomic Eu or atomic O is adsorbed on the bare Ir(111) in the space between the EuO(111) bilayer islands. Through *in vivo* STM experiments, the reaction of adsorbed Eu to EuO in consequence of O₂ exposure was directly followed. The apparent height of EuO(111) bilayer islands with respect to their surroundings strikingly depends on the coadsorbed species and varies from negative apparent thicknesses down to -1.5 Å for coadsorbed Eu to positive ones for coadsorbed O. Extensive work-function measurements show that the variation in the apparent EuO(111) bilayer island thickness is predominantly caused by work-function variations in their surroundings. Experimentally, we estimate the work function of the EuO(111) bilayer on Ir(111) to be $\Phi_{\text{EuO}} \approx 4.2$ eV, substantially larger than the one for the (100) surface of a EuO crystal, but still smaller than the Ir(111) work function. Also, our DFT calculations yield a large work function for the EuO(111) bilayer, although even larger than the Ir(111) one.

With atomic resolution STM imaging, we identify two specific defects in the EuO(111) bilayer: vacancy-type defects, most likely Eu vacancies, and antiphase domain boundaries resulting from the growth-induced coalescence of bilayer islands. The EuO(111) bilayer does not exhibit ferromagnetism down to 45 K.

The EuO(111) bilayer on Ir(111) is the first example of a polar bilayer of a rare-earth metal. Although the properties of the EuO(111) bilayer are, in several respects, similar to the more frequently described polar bilayers of transition metals, it

is unique in its quality and thermal stability. These properties make it an interesting candidate for the toolbox of surface engineering with two-dimensional materials. It is hoped that our comprehensive analysis triggers future work to explore to the properties of other polar bilayers based on rare-earth metals.

ACKNOWLEDGMENTS

The authors acknowledge financial support through Deutsche Forschungsgemeinschaft via Grant No. SFB608. F. Hu thanks the HLRN for computation time. J. Klinkhammer is acknowledged for performing the MOKE measurements.

-
- [1] P. W. Tasker, *J. Phys. C* **12**, 4977 (1979).
- [2] C. Noguera, *J. Phys.: Condens. Matter* **12**, R367 (2000).
- [3] J. Goniakowski, F. Finocchi, and C. Noguera, *Rep. Prog. Phys.* **71**, 016501 (2008).
- [4] C. Noguera and J. Goniakowski, *Chem. Rev.* **113**, 4073 (2013).
- [5] A. Barbier, *Surf. Sci.* **402**, 757 (1998).
- [6] F. Rohr, K. Wirth, J. Libuda, D. Cappus, M. Bäumer, and H.-J. Freund, *Surf. Sci.* **315**, L977 (1994).
- [7] S. Sindhu, M. Heiler, K. M. Schindler, and H. Neddermeyer, *Surf. Sci.* **541**, 197 (2003).
- [8] C. A. Ventrice, T. Bertrams, H. Hannemann, A. Brodde, and H. Neddermeyer, *Phys. Rev. B* **49**, 5773 (1994).
- [9] R. Plass, K. Egan, C. Collazo-Davila, D. Grozea, E. Landree, L. D. Marks, and M. Gajdardziska-Josifovska, *Phys. Rev. Lett.* **81**, 4891 (1998).
- [10] J. Goniakowski, C. Noguera, and L. Giordano, *Phys. Rev. Lett.* **98**, 205701 (2007).
- [11] Y. J. Kim, C. Westphal, R. X. Ynzunza, H. C. Galloway, M. Salmeron, M. A. Van Hove, and C. S. Fadley, *Phys. Rev. B* **55**, R13448 (1997).
- [12] W. Ranke, M. Ritter, and W. Weiss, *Phys. Rev. B* **60**, 1527 (1999).
- [13] M. Kiguchi, S. Entani, K. Saiki, T. Goto, and A. Koma, *Phys. Rev. B* **68**, 115402 (2003).
- [14] W. Hebenstreit, M. Schmid, J. Redinger, R. Podloucky, and P. Varga, *Phys. Rev. Lett.* **85**, 5376 (2000).
- [15] L. Giordano, G. Pacchioni, J. Goniakowski, N. Nilus, E. D. L. Rienks, and H.-J. Freund, *Phys. Rev. B* **76**, 075416 (2007).
- [16] M. De Santis, A. Buchsbaum, P. Varga, and M. Schmid, *Phys. Rev. B* **84**, 125430 (2011).
- [17] F. Sedona, G. A. Rizzi, S. Agnoli, F. X. Llabrés i Xamena, A. Papageorgiou, D. Ostermann, M. Sambri, P. Finetti, K. Schierbaum, and G. Granozzi, *J. Phys. Chem. C* **109**, 24411 (2005).
- [18] C. Tusche, H. L. Meyerheim, and J. Kirschner, *Phys. Rev. Lett.* **99**, 026102 (2007).
- [19] Y. Pan, S. Benedetti, C. Noguera, L. Giordano, J. Goniakowski, and N. Nilus, *J. Phys. Chem. C* **116**, 11126 (2012).
- [20] P. Wachter, *Crit. Rev. Solid State Mater. Sci.* **3**, 189 (1972).
- [21] M. R. Oliver, J. A. Kafalas, J. O. Dimmock, and T. B. Reed, *Phys. Rev. Lett.* **24**, 1064 (1970).
- [22] P. G. Steeneken, L. H. Tjeng, I. Elfimov, G. A. Sawatzky, G. Ghiringhelli, N. B. Brookes, and D.-J. Huang, *Phys. Rev. Lett.* **88**, 047201 (2002).
- [23] T. S. Santos and J. S. Moodera, *Phys. Rev. B* **69**, 241203 (2004).
- [24] M. Müller, G.-X. Miao, and J. S. Moodera, *Europhys. Lett.* **88**, 47006 (2009).
- [25] K. Koike and T. Furukawa, *Phys. Rev. Lett.* **77**, 3921 (1996).
- [26] D. F. Förster, J. Klinkhammer, and T. Michely, *Surf. Sci.* **606**, 1019 (2012).
- [27] Ames Laboratory (Materials Preparation Center) of the US DOE, Iowa State University, Ames, IA 50011-3020.
- [28] D. F. Förster, J. Klinkhammer, C. Busse, S. G. Altendorf, T. Michely, Z. Hu, Y.-Y. Chin, L. H. Tjeng, J. Coraux, and D. Bourgault, *Phys. Rev. B* **83**, 045424 (2011).
- [29] T. Michely, M. Kaiser, and M. J. Rost, *Rev. Sci. Instrum.* **71**, 4461 (2000).
- [30] I. Horcas, R. Fernández, J. M. Gómez-Rodríguez, J. Colchero, J. Gómez-Herrero, and A. M. Baro, *Rev. Sci. Instrum.* **78**, 013705 (2007).
- [31] J. P. Perdew, K. Burke, and M. Ernzerhof, *Phys. Rev. Lett.* **77**, 3865 (1996).
- [32] G. Kresse and J. Hafner, *J. Phys.: Condens. Matter* **6**, 8245 (1994).
- [33] P. E. Blöchl, *Phys. Rev. B* **50**, 17953 (1994).
- [34] G. Kresse and J. Hafner, *Phys. Rev. B* **47**, 558 (1993).
- [35] V. I. Anisimov, F. Aryasetiawan, and A. I. Lichtenstein, *J. Phys.: Condens. Matter* **9**, 767 (1997).
- [36] P. Larson, W. R. L. Lambrecht, A. Chantis, and M. van Schilfgaarde, *Phys. Rev. B* **75**, 045114 (2007).
- [37] H. C. Galloway, J. J. Benitez, and M. Salmeron, *Surf. Sci.* **298**, 127 (1993).
- [38] L. Pauling, *The Nature of the Chemical Bond* (Cornell University Press, New York, 1960).
- [39] G. Barcaro, I. O. Thomas, and A. Fortunelli, *J. Chem. Phys.* **132**, 124703 (2010).
- [40] C. S. Fadley, M. A. van Hove, Z. Hussain, and A. P. Kaduwela, *J. Electron. Spectrosc. Relat. Phenom.* **75**, 273 (1995).
- [41] B. Sachs, T. O. Wehling, M. I. Katsnelson, and A. I. Lichtenstein, *Phys. Rev. B* **84**, 195414 (2011).
- [42] R. Smoluchowski, *Phys. Rev.* **60**, 661 (1941).
- [43] M. Ritter, W. Ranke, and W. Weiss, *Phys. Rev. B* **57**, 7240 (1998).
- [44] M. A. van Hove, W. H. Weinberg, and C.-M. Chan, *Low-Energy Electron Diffraction* (Springer, Berlin, 1986).
- [45] J. Goniakowski, C. Noguera, and L. Giordano, *Phys. Rev. Lett.* **93**, 215702 (2004).
- [46] L. R. Merte, J. Knudsen, L. C. Grabow, R. T. Vang, E. Lægsgaard, M. Mavrikakis, and F. Besenbacher, *Surf. Sci.* **603**, L15 (2009).
- [47] A. D. Novaco and J. P. McTague, *Phys. Rev. Lett.* **38**, 1286 (1977).
- [48] J. P. McTague and A. D. Novaco, *Phys. Rev. B* **19**, 5299 (1979).
- [49] C. G. Shaw, S. C. Fain, and M. D. Chinn, *Phys. Rev. Lett.* **41**, 955 (1978).
- [50] D. F. Förster, T. O. Wehling, S. Schumacher, A. Rosch, and T. Michely, *New J. Phys.* **14**, 23022 (2012).
- [51] L. Olesen, M. Brandbyge, M. R. Sørensen, K. W. Jacobsen, E. Lægsgaard, I. Stensgaard, and F. Besenbacher, *Phys. Rev. Lett.* **76**, 1485 (1996).

- [52] See Supplemental Material at <http://link.aps.org/supplemental/10.1103/PhysRevB.89.115410> for additional work-function measurements by means of the Gundlach oscillations.
- [53] V. P. Ivanov, G. K. Boreskov, V. I. Savchenko, W. F. Egelhoff, Jr., and W. H. Weinberg, *Surf. Sci.* **61**, 207 (1976).
- [54] R. W. Strayer, W. Mackie, and L. W. Swanson, *Surf. Sci.* **34**, 225 (1973).
- [55] K. Jakobi, *3.1.2.4 Work Function Data*, Landolt-Börnstein, Group III, Condensed Matter, Vol. 24b (Springer, Berlin, 1994).
- [56] G. Busch, P. Cotti, and P. Munz, *Solid State Commun.* **7**, 795 (1969).
- [57] D. E. Eastman, F. Holtzberg, and S. Methfessel, *Phys. Rev. Lett.* **23**, 226 (1969).
- [58] J. Goniakowski, L. Giordano, and C. Noguera, *Phys. Rev. B* **81**, 205404 (2010).
- [59] E. D. L. Rienks, N. Nilius, H.-P. Rust, and H.-J. Freund, *Phys. Rev. B* **71**, 241404 (2005).
- [60] N. Nilius, S. Benedetti, Y. Pan, P. Myrach, C. Noguera, L. Giordano, and J. Goniakowski, *Phys. Rev. B* **86**, 205410 (2012).
- [61] S. Schumacher, T. O. Wehling, P. Lazić, S. Runte, D. F. Förster, C. Busse, M. Petrović, M. Kralj, S. Blügel, N. Atodiresei, V. Caciuc, and T. Michely, *Nano Lett.* **13**, 5013 (2013).
- [62] J. Knudsen, L. R. Merte, L. C. Grabow, F. M. Eichhorn, S. Porsgaard, H. Zeuthen, R. T. Vang, E. Lægsgaard, M. Mavrikakis, and F. Besenbacher, *Surf. Sci.* **604**, 11 (2010).
- [63] Y. Yao, Q. Fu, Z. Wang, D. Tan, and X. Bao, *J. Phys. Chem. C* **114**, 17069 (2010).
- [64] E. J. Huber and C. E. Holley, *J. Chem. Thermodyn.* **1**, 301 (1969).
- [65] O. Dulub, U. Diebold, and G. Kresse, *Phys. Rev. Lett.* **90**, 016102 (2003).
- [66] R. Schiller and W. Nolting, *Phys. Rev. Lett.* **86**, 3847 (2001).
- [67] J. Klinkhammer, D. F. Förster, S. Schumacher, H. P. Oepen, T. Michely, and C. Busse, *Appl. Phys. Lett.* **103**, 131601 (2013).